electronics

Article

Explainable Intelligent Inspection of Solar Photovoltaic Systems with Deep Transfer Learning: Considering Warmer Weather Effects Using Aerial Radiometric Infrared Thermography

Usamah Rashid Qureshi [1,*], Aiman Rashid [2,3], Nicola Altini [1,*], Vitoantonio Bevilacqua [1] and Massimo La Scala [1]

[1] Department of Electrical and Information Engineering, Polytechnic of Bari, 70126 Bari, BA, Italy; vitoantonio.bevilacqua@poliba.it (V.B.); massimo.lascala@poliba.it (M.L.S.)
[2] Department of Industrial Engineering, University of Florence, 50121 Florence, FI, Italy; aiman.rashid@unifi.it
[3] Department of Electrical and Electronic Engineering, University of Cagliari, 09124 Cagliari, CA, Italy
* Correspondence: usamahrashid.qureshi@poliba.it (U.R.Q.); nicola.altini@poliba.it (N.A.)

Abstract: Solar photovoltaic (SPV) arrays play a pivotal role in advancing clean and sustainable energy systems, with a worldwide total installed capacity of 1.6 terawatts and annual investments reaching USD 480 billion in 2023. However, climate disaster effects, particularly extremely hot weather events, can compromise the performance and resilience of SPV panels through thermal deterioration and degradation, which may lead to lessened operational life and potential failure. These heatwave-related consequences highlight the need for timely inspection and precise anomaly diagnosis of SPV panels to ensure optimal energy production. This case study focuses on intelligent remote inspection by employing aerial radiometric infrared thermography within a predictive maintenance framework to enhance diagnostic monitoring and early scrutiny capabilities for SPV power plant sites. The proposed methodology leverages pre-trained deep learning (DL) algorithms, enabling a deep transfer learning approach, to test the effectiveness of multiclass classification (or diagnosis) of various thermal anomalies of the SPV panel. This case study adopted a highly imbalanced 6-class thermographic radiometric dataset (floating-point temperature numerical values in degrees Celsius) for training and validating the pre-trained DL predictive classification models and comparing them with a customized convolutional neural network (CNN) ensembled model. The performance metrics demonstrate that among selected pre-trained DL models, the MobileNetV2 exhibits the highest F1 score (0.998) and accuracy (0.998), followed by InceptionV3 and VGG16, which recorded an F1 score of 0.997 and an accuracy of 0.998 in performing the smart inspection of 6-class thermal anomalies, whereas the customized CNN ensembled model achieved both a perfect F1 score (1.000) and accuracy (1.000). Furthermore, to create trust in the intelligent inspection system, we investigated the pre-trained DL predictive classification models using perceptive explainability to display the most discriminative data features, and mathematical-structure-based interpretability to portray multiclass feature clustering.

Keywords: radiometric infrared thermography; solar photovoltaic panel; intelligent inspection; predictive maintenance; intelligent fault detection and diagnosis; explainable artificial intelligence

Academic Editor: Francisco Javier Ruiz-Rodríguez

Received: 16 January 2025
Revised: 8 February 2025
Accepted: 10 February 2025
Published: 14 February 2025

Citation: Qureshi, U.R.; Rashid, A.; Altini, N.; Bevilacqua, V.; La Scala, M. Explainable Intelligent Inspection of Solar Photovoltaic Systems with Deep Transfer Learning: Considering Warmer Weather Effects Using Aerial Radiometric Infrared Thermography. *Electronics* **2025**, *14*, 755. https://doi.org/10.3390/electronics14040755

1. Introduction

The share of renewables in total final energy consumption (TFEC) constituted 28.2% of the worldwide electricity sector in 2021 and topped the 30% mark (≈8932 terawatt-hours) in

2023, with the total installed capacity of solar photovoltaics (SPV) reaching 1.624 terawatts in 2023 (38% > 1.177 terawatts in 2022), corresponding to about 40% of 4.085 terawatts, which is projected to surpass two terawatts by the end of 2024 [1–5]. With a 25-year economic life span, utility-scale SPV power projects commissioned in 2023 had a global weighted average total-capacity installation cost of USD 758/kW (16.5% < USD 908/kW in 2022). The levelized cost of electricity (LCOE) was USD 0.044/kWh (12% < USD 0.050/kWh in 2022) [6].

In 2023, the global net addition to renewable power generating capacity installed was 576 gigawatts, with the dominant grid-connected SPV share representing 78% (447 gigawatts) [4]. The European Union (EU 27) added 53.124 gigawatts, achieving a cumulative installed SPV capacity of 256.911 gigawatts, thus exceeding 44% of total EU renewable electricity generation share in its regional energy mix [7–9].

According to the market exchange rate (MER) in 2023, global annual investments in SPV power generation grew to USD 480 billion, exceeding the combined investments in all other electricity generation technologies, including fossil fuels (oil, natural gas, coal) and other energy sources (hydro, wind, nuclear), which totalled USD 413 billion [10].

Furthermore, 2023 was observed as the hottest year on record [11–13]. SPV arrays are directly exposed to climate change effects, i.e., global warming. In particular, spells of heatwave and persistent heat domes are among the most lethal weather phenomena, acting as risk multipliers to raise the probability of thermally induced defects and substantiate cascading impacts of disastrous failure [14–21]. As the worldwide climate crisis escalates, intensely high temperatures soaring beyond 40 °C and topping 50 °C have become more frequent and continuous across various geographic regions, undermining critical systems and paralyzing vital infrastructure essential for public health and safety.

1.1. Global Warming and Escalated Electric Power Demands

Scorching heatwaves are becoming more prevalent and intense, starting earlier, ending later, and affecting multiple areas simultaneously [22,23]. Notable instances of severe, frequent, and prolonged heatwaves have recently occurred in southern Europe and north Africa, with sustained temperatures of 48.2 °C on 24 July 2023 in Lotzorai and Jerzu (Sardinia, Italy), and Agadir (Morocco) recording 50.4 °C on 11 August 2023 [24]. Such exacerbating heatwaves pose a global threat, significantly shaping the humanitarian landscape of the 21st century [25].

Asia, in particular, has experienced faster warming than the global average, with the warming trend nearly doubling between 1961 and 1990 [14,25–27]. The multifaceted impacts of extreme heat ripple across various sectors through interconnected pathways, significantly affecting agriculture, health, water resources, economy, livability, critical infrastructure, and the environment [22,28–30]. For instance, extreme heat challenges the endurance and resilience of critical electric power generation infrastructure by elevating electricity demand to feed refrigeration, air conditioning, and cooling fans. This increased demand poses significant risks of targeted energy supply disruptions due to systematic overloading, particularly at times when it is most needed to access essential services [31–33]. The interplay of infrastructure failures and electric supply crises during extreme heat events can escalate heatwave burden into full-blown emergencies, which can cause delays and interruptions in humanitarian response efforts, such as sustaining power-dependent cold storage facilities for essential life-saving operations, medications, and vaccinations [23].

1.2. Warmer Weather Effects and Thermal Degradation

Extreme heat can have several detrimental effects on solar photovoltaic (SPV) panels [34]: (i) reduced efficiency, since high temperatures interfere with the panels' ability to convert sunlight into electricity efficiently, hindering optimal operation of SPV energy systems; (ii) thermal degradation, where the materials within the panels deteriorate, diminishing power output and causing physical damage to crucial components; (iii) potential for hotspots, causing damage that can spread, jeopardizing the structural integrity of the panels; (iv) accelerated aging and failure risk, increasing maintenance costs and necessitating earlier-than-expected thorough inspection and replacements.

Early-warning and early-action systems for climate-resilient electricity infrastructure such as smart monitoring and maintenance based on AI are crucial to mitigate heat-related risks [21]. Inspection (BS EN 13306:2017) plays a pivotal role in maintaining the SPV arrays' targeted electrical power generation output through periodic observation and testing [35]. Intelligent remote inspection (IRI) systems employing drone-aided thermographic imaging can continuously track SPV panel temperatures and conduct periodic diagnostic monitoring to precisely identify and address heat-induced issues promptly [31].

1.3. SPV Power Systems and Intelligent Radiometric Thermographic Inspection

The field of fault diagnosis for solar photovoltaic (SPV) panels using infrared thermography (IRT) has seen significant progress, but several critical gaps remain that limit its full potential. One of the primary challenges is the limited generalization of existing models due to the scarcity of faulty IRT datasets [36], as SPV power systems are expected to operate under healthy conditions achieving targeted output continuously, resulting in fewer thermal faulty data instances. Thus, the key issue is the imbalance in fault datasets, where anomalies like hotspot faults or heated junction box failures are often underrepresented, leading to biased models that tend to predict the more frequent No-Anomaly class with greater accuracy. Many existing systems also focus solely on binary classification (No-Anomaly vs. Anomaly), failing to distinguish between multiple types of faults, which is critical for accurate diagnostic monitoring and maintenance. To comply with standards (IEC TS 62446-3:2017) [37] for outdoor IRT of SPV modules in a Predictive Maintenance (PdM) framework for automatic diagnosis, intelligent radiometric thermographic inspection plays a vital role in the early identification of thermal anomalies. Finally, the lack of transferable and pre-trained models means that each fault detection system must be built from scratch, requiring large, labeled datasets and high computational resources, which are often impractical in real-world scenarios.

1.4. Pre-Trained Deep Learning and Diagnostic Monitoring

Pre-trained deep learning (DL) models, particularly when trained on ImageNet [38] datasets, present a powerful solution to these challenges, offering a robust framework for both binary classification (No-Anomaly vs. Anomaly) and multi-class classification (No-Anomaly vs. multiple fault categories) [39]. By leveraging pre-trained feature extractors from large-scale datasets like ImageNet [38], DL models significantly improve generalization capabilities, even when the training data for SPV faults are limited for diagnostic monitoring. In the paradigm of Deep Transfer Learning (DTL), the models can transfer the patterns learned from a wide range of images to specific tasks, such as the diagnosis of IRT images of SPV panels, enabling them to accurately detect faults with much smaller amounts of domain-specific data. Furthermore, DL models, such as VGG16 [40,41], eliminate the need for traditional feature engineering by automatically extracting relevant features from the IRT images. In addition to simplifying the feature selection process, DTL also allows for faster training and more accurate classification.

DTL can be also used in cases of class imbalance or skewed datasets, a common issue in fault detection tasks [39]. In this case, it should be used in conjunction with techniques like data augmentation, oversampling, and class-weighted loss functions, ensuring that minority fault classes receive adequate attention during training [42]. This results in more accurate predictions, particularly for rare faults, which are often overlooked when no corrective methods are applied.

1.5. Motivation and Contribution

Conventionally, SPV power plants consist of one or more SPV arrays, integrated with protective anti-reverse diodes and conventional electrical converters and inverters that enable connection to local grids or loads. Traditional approaches were developed to identify particular fault types in SPV systems, with some methods necessitating the disconnection of SPV panels, thereby interrupting overall energy production [39]. The considered aerial radiometric IRT dataset is tailored for industrial supervision, operation/vision inspection, and diagnostic monitoring, without interruption or disconnection of utility electric power generation. The adoption of automatic diagnostic models enables the PdM paradigm, which enhances SPV array performance by detecting potential problems before they manifest, ensuring the longevity and reliability of both large-scale and utility-scale SPV energy systems, and safeguarding their invested capital, despite increasing and prolonged heatwave occurrences [43].

The main contribution of this case study is twofold: (i) to further explore the efficacy of the selected pre-trained DL models fed with the tailored radiometric dataset for intelligent inspection; (ii) to employ explainability techniques to DL models for intelligent fault diagnosis (IFD).

In this work, we leveraged the DTL approach, which consists of employing DL models pre-trained on datasets such as ImageNet [38] for the specific task under consideration [44]. Particularly, we benchmarked 10 DTL models, which were developed over a span of eight years, and compared them with a custom convolutional neural network (CNN) ensembled model elaborated with explainable artificial intelligence (XAI) visualizations.

2. Related Works

Various pre-trained DL models/algorithms based on CNNs were applied for DTL to classify SPV panel IRT image anomalies. The existing approaches are summarized in this section.

Haidari et al. exploited infrared (IR) thermal images of 3-class (healthy, hotspot, and hot substring) having 70×50 pixels and preprocessed them with median blurring and grayscale conversion by Adobe Photoshop® and applied a pre-trained model (VGG-16) to achieve 0.980 fault classification accuracy [41].

Le and others considered grayscale images of 12-class having 24×40 pixels and preprocessed them using augmentation (flipping: horizontal and vertical; $\pm 20\%$ size translation) and the optional synthetic minority oversampling technique (SMOTE), and applied a pre-trained model (ResNet50) to an ensemble of 15 models employing a combination of methods to achieve 0.860 fault classification accuracy [45].

Korkmaz and Acikgoz considered grayscale images of 12-class having 24×40 pixels and preprocessed them using augmented oversampling ($\pm 30\%$ brightness, reverse $\times$ 2, $180°$ rotation $\times$ 1), and applied a pre-trained model (AlexNet) for multiscale transfer learning (TL) with three parallel branches on selected 11-class images to achieve 0.935 fault classification accuracy [46].

Duranay investigated grayscale images of 12-class having 24×40 pixels and preprocessed them (image resize: 224×224, exemplar patches: 28×28 and 56×56) and applied a pre-trained model (EfficientNet B0) with a feature selector using neighborhood component analysis (NCA), a support vector machine (SVM) as classifier, and a 10-fold cross-validation algorithm, achieving a 0.939 fault classification accuracy [47].

Pamungkas exploited grayscale images of 12-class having 24 × 40 pixels and pre-processed them by augmentation (geometric transformation and generative adversarial network—GAN) and applied a pre-trained model (coupled UDenseNet), achieving a 0.957 fault classification accuracy [48].

Ahmed presented a hybrid local features-based approach for SPV system monitoring using infrared thermographs, addressing key challenges like scaling, noise, rotation, and haze. By subdividing images into 5 × 5 pixel grids and using unsupervised clustering, the method enhances robustness while reducing memory usage. It achieves 0.980 training accuracy and 0.968 testing accuracy with high precision, recall, and F1 scores, ensuring reliable classification of faulty, healthy, and hotspot states [49].

Ramadan et al. proposed a DL-based fault detection system using the Infrared Solar Modules dataset (12-class grayscale) and a Transformer ANN approach. Preprocessing includes sharpening filters and oversampling augmentation to enhance and balance the dataset. A ViT-based model classifies PV anomalies, achieving 0.982 accuracy for two classes, 0.962 for 11 faults, and 0.956 for 12 classes [50].

Mellit et al. compared five hybrid DCNN-ML classifiers by first training a deep CNN for feature extraction on a 4-class dataset and then integrating different ML classifiers. Support Vector Machine (SVM) and XGBoost achieved an accuracy of 0.870, outperforming Random Forest (0.860), k-Nearest Neighbors (0.840), and Decision Tree (0.810) [51].

Ksira et al. proposed a low-cost, low-power embedded system (Arduino Nano 33 BLE sense) for solar PV module fault diagnosis using IRT images (5-class, 32 × 24 pixels) and TinyCNN. The TinyCNN model is converted into TF Lite, Float 16, and Dynamic Range Optimization (DRO) for quantized mode. The model achieved 0.815 to 0.948 accuracy, but experimental accuracy drops due to the low-resolution IR camera. The system, costing $120, enables real-time, local fault detection without cloud processing or expert intervention, aiding non-experts in predictive maintenance [52].

Wang et al. introduced Photovoltaic Fault (PVF-10), an open-source unmanned air vehicle (UAV) IRT image dataset with 5579 cropped PV panel images from eight plants, categorized into 10 fault types. Among five DL (ResNet50, EfficientNetV2S, Vision Transformer-S, Swin Transformer V2-Tiny, and Co-scale Conv-attentional image Transformers [Coat-Lite Small]) models, the Coat (CNN Transformer hybrid) achieved the highest accuracy (0.933) [53].

In our previous work, a radiometric image dataset (a floating-point temperature intensity matrix in degrees Celsius) of imbalanced 6-class images, each measuring 60 × 100 pixels, was preprocessed by zero-padding and visual diversity augmentation (horizontal and vertical flipping) with an option of dataset balancing (employing SMOTE). We applied a customized CNN model with ensembled stratified fourfold cross-validation to achieve perfect classification accuracy (1.000), elaborated by explainable artificial intelligence techniques [54].

3. Materials and Methods

3.1. Dataset Selection

This case study adopted a severely imbalanced 6-class radiometric IRT dataset of SPV panels (2672 instances) comprising floating-point temperature numerical values in degrees Celsius (temperature intensity matrix), with a dimension of 60 × 100 datapoints for DTL-based multiclass classification (or thermal anomaly diagnosis), as shown in Figure 1. The dataset comprises one "Good" class of majority instances (2647) and five "Faulty" classes of minority instances (having five instances under each minority class). The five minority classes were labeled as heated Junction Box, Hotspot effect, Patchwork pattern, faulty Substring, and faulty Multistring [54].

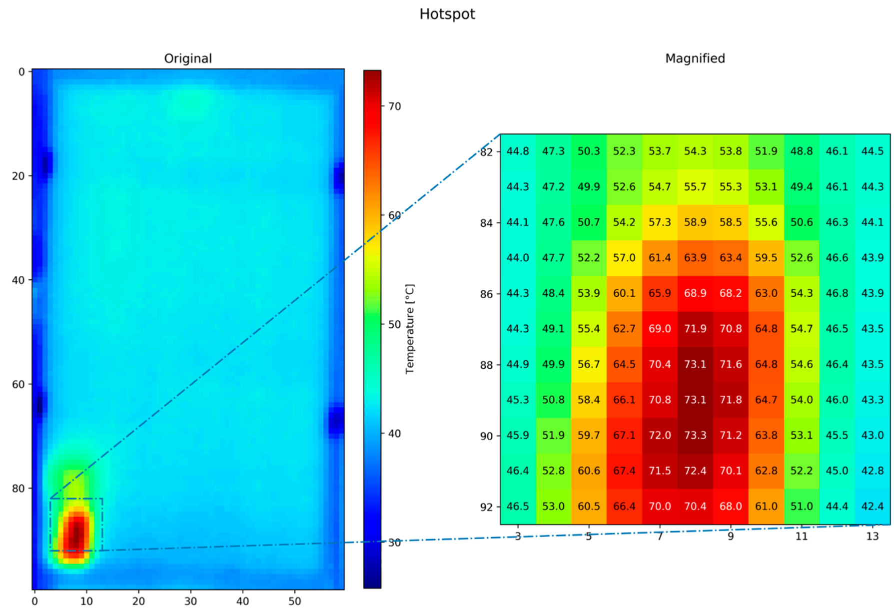

Figure 1. Solar PV panel labeled Hotspot effect: Original and magnified region of 2D radiometric datapoints—temperature intensity matrix [°C] (jet colormap as pseudo-color applied for visual depiction).

3.2. Experimental Workflow

The experimental workflow consisted of four main steps: (i) Input: preparing the radiometric IRT-SPV dataset; (ii) Individuation of 10 DTL models and our custom CNN model; (iii) Modification of the DTL models to perform fine-tuning; (iv) Output: performance measure. The experimental workflow is illustrated in Figure 2.

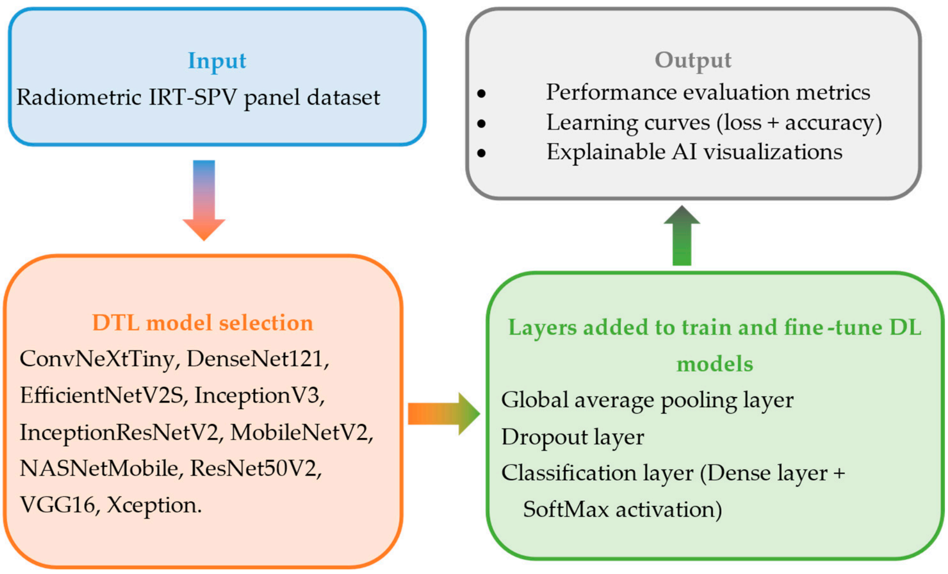

Figure 2. Experimental workflow (simplified block diagram).

For DTL, the following pre-trained DL models were applied, including our customized CNN (ensembled) model, as shown in Table 1, along with Top-1 and Top-5 accuracies of each DL model as demonstrated on the ImageNet dataset [38].

Table 1. List of DL models. Top-1 and Top-5 accuracies are reported on the ImageNet dataset [38].

Model	Year	Size (MB)	Parameters	Depth	Top-1 Accuracy	Top-5 Accuracy
ConvNeXtTiny [55]	2022	109.42	28.6 M	-	0.813	-
DenseNet121 [56]	2017	33	8.1 M	242	0.75	0.923
EfficientNetV2S [57]	2021	88	21.6 M	-	0.839	0.967
InceptionV3 [58]	2016	92	23.9 M	189	0.779	0.937
InceptionResNetV2 [59]	2017	215	55.9 M	449	0.803	0.953
MobileNetV2 [60]	2018	14	3.5 M	105	0.713	0.901
NASNetMobile [61]	2018	23	5.3 M	389	0.744	0.919
ResNet50V2 [62]	2016	98	25.6 M	103	0.760	0.930
VGG16 [63]	2015	528	138.4 M	16	0.713	0.901
Xception [64]	2017	88	22.9 M	81	0.790	0.945
Custom CNN [54]	2024	1.80	0.471 M	5	-	-
Ensembled Model [54]	2024	7.19	1.89 M	5	-	-

In the realm of PdM, intelligent inspection and fault diagnosis offer an effective and viable solution that saves time, reduces costs, minimizes labor, inefficiently supervising and monitoring large industrial plant processes and energy generation managerial operations for targeted outcomes [43,65].

The highly imbalanced input dataset was distributed proportionately as 60% training, 20% validation, and 20% testing, revealing that only one data instance was available for testing in each of the five minority classes for multiclass classification, which is a challenging process for any DTL model, akin to finding a needle in a haystack. Each pre-trained DL model was separately selected for DTL with added layers (i.e., global average pooling/flatten layer, dropout rate 0.5, dense layer with SoftMax activation function [66]) to fine-tune the prediction of 6-class classification (or thermal fault diagnosis), as illustrated in Figure 2.

The following options were employed for the hyperparameter tuning: epochs 1000, batch size 512, early stopping with patience of 200 (monitor: minimizing validation loss, minimum delta: 0.001), Lion optimizer [67,68] with learning rate 0.0001, categorical cross-entropy as loss function, and class-weights applied to resolve the class imbalance. The performance evaluation metrics demonstrated the multiclass classification output.

3.3. Deep Learning Models

A brief description of each considered CNN model is provided here.

ConvNeXtTiny [55] is inspired by the principles of the Vision Transformer (ViT) while retaining the simplicity of convolutional architectures. By adopting design elements such as inverted bottlenecks, depth-wise convolutions, and layer normalization, this model aligns CNN closer to transformer performance while preserving computational efficiency, aiming to blend CNN robustness with transformer-like scalability.

DenseNet121 [56] introduces a breakthrough approach to connectivity by establishing direct connections between each layer and all subsequent layers in a feed-forward manner, addressing the vanishing gradient problem efficiently. This dense connectivity pattern encourages feature reuse, leading to more compact and efficient models with fewer parameters that emphasize model performance with parameter efficiency in resource-constrained scenarios.

EfficientNetV2S [57] utilizes progressive learning to balance accuracy and efficiency by scaling networks with a combination of neural architecture search (NAS) and compound scaling. It introduces improved speed and memory efficiency compared to its predecessor, EfficientNet, and serves as a forward-thinking framework that could be foundational in deploying real-time applications in resource-limited environments like mobile and edge devices.

InceptionV3 [58] builds upon its predecessors by introducing factorized convolutions and aggressive dimensionality reduction, leading to highly optimized computational performance without compromising accuracy. Its mix of convolutional filter sizes promotes multi-level feature extraction, which is ideal for complex image classification tasks where interpretability across scales is critical. It inspires modular design, offering a hybrid of computational economy and structural depth.

InceptionResNetV2 [59] merges the strengths of both inception modules and residual connections, creating a model capable of deeper network training without degradation in performance. By combining the versatility of inception blocks with the stability of residual learning, this architecture stands for hybrid models pushing boundaries in both accuracy and depth. Its critical advantage lies in reconciling efficient multi-level feature capture with the benefits of bypassing unnecessary gradient flow disruptions.

MobileNetV2 [60] introduces the concept of inverted residuals and linear bottlenecks to drastically reduce the computational and memory footprint while maintaining high performance, specifically tailored for mobile and embedded device applications. Its lightweight design, coupled with the strong representational power of depth-wise separable convolutions, offers a balance between deployment feasibility and accuracy for real-time inference applications.

NASNetMobile [61], an offshoot of neural architecture search (NAS), represents an automated approach to model architecture optimization, specifically for mobile low-power applications. It strikes a balance between precision and efficiency by employing reinforcement learning techniques to identify optimal network structures. The architecture is a steppingstone toward automating CNN design that revolutionizes personalized and domain-specific neural networks with minimal manual intervention.

ResNet50V2 [62] refines the original ResNet by modifying the ordering of batch normalization and activations within residual blocks, improving model training stability and convergence speed. Its key contribution lies in deep residual learning, which effectively mitigates the performance degradation problem in very deep networks and is suited for scalability with gradient flow control.

VGG16 [63] is a pioneering deep network architecture, characterized by its simplicity and depth, relying solely on 3×3 convolutional layers stacked deeply for feature extraction. Despite its relatively large parameter size, the sequential and uniform architecture of VGG16 has made it an intuitive model to enhance simplicity in design while exploring more sophisticated techniques for parameter reduction.

Xception [64] extends the concept of depth-wise separable convolutions to an extreme, introducing a fully convolutional architecture without any intermediate fully connected layers. The structure is simple and powerful, leveraging the efficiency of separable convolutions while preserving a high degree of representational capability, and exploring extreme model optimization in scenarios requiring the balance of computational load with high-dimensional feature learning.

Custom CNN [54] is based on three blocks of layers (conv2d, batch normalization, maxpooling2d), increasing kernel size 3×3, 5×5, and 7×7, two dense layers, and a global-max-pooling2d layer that makes for a lightweight and efficient CNN model.

The core ideas, strategies, and methods of the DL models are tabulated in Table 2.

Table 2. DL models: strategies and methods.

Model	Core Ideas	Strategies	Methods
ConvNeXtTiny [55]	A modernized CNN architecture that adapts transformer-inspired design principles for improved efficiency and performance.	Leverages depth-wise convolutions, layer normalization, residual connections, and simplified block design.	Replaces batch normalization with layer normalization, uses fewer activation functions, incorporates larger kernel sizes (7×7), and minimizes unnecessary complexity while maintaining CNN efficiency.
DenseNet121 [56]	Densely connected convolutional networks that enhance gradient flow and parameter efficiency.	Uses dense connectivity, where each layer is connected to all preceding layers, reducing vanishing gradients.	Features compact parameterization, improved feature reuse, and reduced redundancy by concatenating outputs instead of summing them.
EfficientNetV2S [57]	A scalable CNN that balances efficiency and accuracy using Neural Architecture Search (NAS).	Introduces compound scaling for width, depth, and resolution, and uses the Inverted Residual Block (fused MBConv) approach to improve computational efficiency.	Uses a progressive learning strategy, smaller convolutional kernels, and improved regularization to accelerate training and inference.
InceptionV3 [58]	A refined version of Inception networks optimized for better computational efficiency.	Uses factorized convolutions, asymmetric convolutions, and auxiliary classifiers to improve gradient propagation.	Employs label smoothing, batch normalization, and RMSProp optimizer to enhance learning stability and performance.
InceptionResNetV2 [59]	A hybrid model combining the benefits of Inception modules and residual connections.	Integrates residual connections within Inception blocks to allow deeper networks without vanishing gradients.	Employs factorized convolutions, batch normalization, and lower parameter usage compared to ResNets of similar depth.
MobileNetV2 [60]	A lightweight model designed for mobile and edge computing with minimal computational cost.	Introduces inverted residual blocks with linear bottlenecks to maintain low complexity while preserving accuracy.	Uses depth-wise separable convolutions, ReLU activation, and optimized width multipliers to adjust resource efficiency.
NASNetMobile [61]	A model designed using Neural Architecture Search (NAS) to optimize efficiency and accuracy of mobile devices.	Leverages reinforcement learning-based NAS to discover efficient architectures.	Uses separable convolutions, optimized cell structures, and progressive learning strategies for low-latency inference.
ResNet50V2 [62]	A refined deep residual network (ResNet) variant that enhances training stability and performance.	Uses improved residual connections with pre-activation layers to mitigate vanishing gradients.	Applies identity mappings, batch normalization before activation, and deep residual learning to improve convergence.
VGG16 [63]	A simple yet powerful CNN architecture with uniform layers and large kernel filters.	Employs a deep stack of 3×3 convolutional layers with max pooling for feature extraction.	Uses deep sequential layers, uniform filter size, and fully connected layers for robust image classification.
Xception [64]	An extension of the Inception architecture that fully utilizes depth-wise separable convolutions.	Replaces standard convolutions with depth-wise separable convolutions to improve efficiency and reduce parameters.	Uses residual connections, batch normalization, and efficient spatial-channel decoupling for better learning capacity.

Table 2. *Cont.*

Model	Core Ideas	Strategies	Methods
Custom CNN [54]	A light-weight model to classify highly imbalanced datasets.	Uses standard convolution layers with progressive increments of kernel size to extract coarse and fine features of images.	Based on three blocks of layers (conv2d, batch normalization, maxpooling2d), increasing kernel sizes of 3 × 3, 5 × 5, and 7 × 7, two dense layers, and a global-max-pooling2d layer to improve efficiency.

3.4. Performance Evaluation Metrics

The performance evaluation metrics provide a comprehensive quantitative evaluation of the DTL model predictions to perform multiclass classification, including accuracy, precision, recall, F1 score, and training time (in seconds).

The learning curves in Figure 3 serve as a behavioral illustration monitoring the learning progress and performance of the DTL models over time. As the number of epochs or training iterations increases, these learning curves help to portray a well-fit model when both training and validation sets show consistent improvement that generalizes effectively.

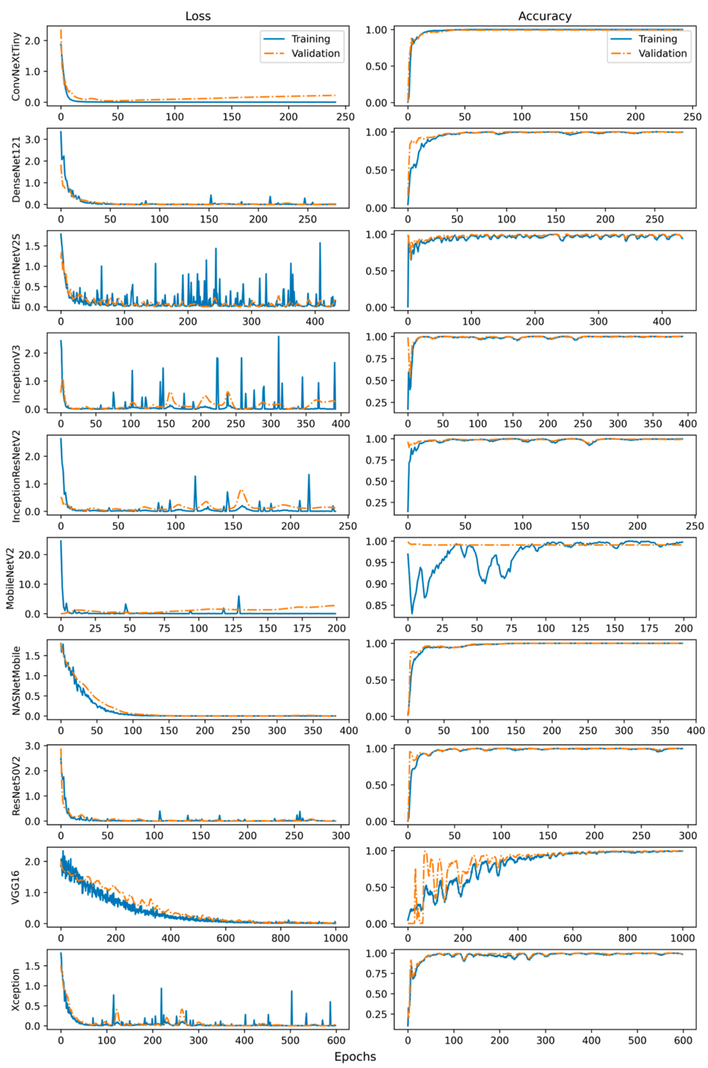

Figure 3. Learning curves of DTL models (6-class).

3.5. Explainable Artificial Intelligence Methods

The quest for explainability and interpretability in DL models has led to the emergence of explainable artificial intelligence (XAI) techniques [69], which are pivotal in demystifying the decision-making processes of these complex systems [70]. Broadly, XAI methods are categorized into two complementary approaches [71–73]: perceptive explainability and mathematical interpretability. Perceptive explainability provides visual insights such as saliency maps or feature attributions, which align closely with human intuition and cognitive understanding, and facilitate immediate comprehension of model behavior. In contrast, mathematical interpretability delves into the underlying logic covering the mathematical constructs and relationships that define the model's input data representation. Together, these approaches foster a holistic understanding of DL models, bridging the gap between their technical intricacies and practical transparency, thereby promoting trust, accountability, and further refinement in their application.

3.5.1. Perceptive Explainability

The primary goal of XAI methods within the domain of perceptive explainability is to offer clear and intuitive visual representations of the most influential features driving a model's predictions. These methods focus on identifying and highlighting regions or attributes within the input data that significantly impact the decision-making process of the model by visually mapping the contributions of specific features. Perceptive explainability enables a deeper understanding of feature-level classification behavior. This approach is instrumental in analyzing the relevance of particular regions or elements of the input data, providing valuable insights into the model's reasoning and further facilitating improved interpretability and trustworthiness in its predictions. The SmoothGrad technique [74,75] is applied in this study to realize perceptive explainability mappings with the Guided Backpropagation method [76] for enhanced visualizations.

Simonyan et al. [74] introduced image-specific class saliency visualization, a technique aimed at identifying which parts of an image most influence the deep CNN's predictions. In the context of linear models, larger weight values correspond to more significant features. However, in highly nonlinear models like deep CNNs, the first-order Taylor expansion is employed to approximate the model's behavior, allowing for saliency map generation. Despite their utility, these initial maps were often noisy. To improve upon this, Smilkov et al. [75] proposed the SmoothGrad method, which averaged multiple noisy perturbations of an image to produce smoother, more interpretable saliency maps. Meanwhile, Springenberg et al. [76] introduced the Guided Backpropagation (GBP) method, which adds a guiding signal from higher layers during backpropagation, effectively blocking the flow of negative gradients that correspond to neurons that decrease the activation of the target higher layer unit. Hence GBP complements SmoothGrad, resulting in cleaner and sharper visualizations that provide more accurate and intuitive insights into the model's decision-making process. Here, 25 smooth samples are employed to compute SmoothGrad.

3.5.2. Mathematical Interpretability

Mathematical interpretability methods aim to uncover the inner workings of all models by leveraging mathematical structures to explain how information is processed, and features are utilized for predictions. These methods provide crucial insights into the clustering and categorization capabilities of neural networks, revealing how data is grouped and organized. Such analyses enable researchers to evaluate whether the features learned by the model are meaningful and relevant to the specific task at hand. In this research, Uniform Manifold Approximation and Projection (UMAP) [77] is employed as the mathematical interpretability technique. UMAP is a nonlinear dimensionality reduction method founded on three core assumptions: (i) data is uniformly distributed along a manifold, (ii) the manifold's topological structure is preserved, and (iii) the manifold is locally connected. The method operates in two main stages: first, it learns the structure of the high-dimensional manifold; then, it maps this structure onto a lower-dimensional space. By applying UMAP to the predicted features' output, the study effectively visualizes feature clustering, offering a detailed understanding of how the model processes and categorizes information. This approach enhances interpretability by making the models' learned representations more accessible and comprehensible.

3.6. Experimental Resources

The experimental simulations were performed by accessing paid version resources of Google Colab (available online: https://colab.research.google.com/, last accessed on 30 January 2025).

The software environment is based on Python (v. 3.11.11) and Keras (v. 3.5.0) frameworks with TensorFlow (v. 2.17.1) at the backend to apply pre-trained DL models (online available: https://keras.io/api/applications/, last accessed on 30 January 2025). The performance evaluation and analyses employed the scikit-learn (v. 1.6.1) library. The explainable predictive visualizations exploited the tf-keras-vis (v. 0.8.7) library.

4. Results and Discussion

This section presents the experimental results and findings of the chosen DTL models and the custom CNN model for performance evaluation of predictions and trainingvalidation behavior through learning curves.

The data in Table 1 provide insights into the structural complexities of the models; architectural characteristics and factors such as model size, parameter count, and depth are critical and directly influence their performance (as reported in Tables 3 and 4), resource consumption, and suitability for various tasks.

Table 3. Model performance for 6-class classification.

Model	Accuracy	Precision	Recall	F1 Score	Training Time (Sec)
ConvNeXtTiny [55]	0.994	0.989	0.994	0.992	1068
DenseNet121 [56]	0.994	0.993	0.994	0.993	742
EfficientNetV2S [57]	0.996	0.993	0.996	0.995	2894
InceptionV3 [58]	0.998	0.996	0.998	0.997	326
InceptionResNetV2 [59]	0.994	0.993	0.994	0.993	537
MobileNetV2 [60]	0.998	0.999	0.998	0.998	1095
NASNetMobile [61]	0.996	0.996	0.996	0.996	1907
ResNet50V2 [62]	0.996	0.993	0.996	0.995	511
VGG16 [63]	0.998	0.996	0.998	0.997	2529
Xception [64]	0.996	0.993	0.996	0.995	1733
Custom CNN [54]	1.000	1.000	1.000	1.000	204

Table 4. Model performance for 5-class classification. These results are computed from the previous models (trained for 6-class classification) but considering only anomaly classes.

Model	Accuracy	Precision	Recall	F1 Score
ConvNeXtTiny [55]	0.960	1.000	1.000	1.000
DenseNet121 [56]	0.960	1.000	1.000	1.000
EfficientNetV2S [57]	0.960	0.958	0.950	0.949

Table 4. *Cont.*

Model	Accuracy	Precision	Recall	F1 Score
InceptionV3 [58]	0.920	0.958	0.900	0.922
InceptionResNetV2 [59]	0.840	0.917	0.900	0.904
MobileNetV2 [60]	0.960	1.000	0.950	0.972
NASNetMobile [61]	0.960	1.000	1.000	1.000
ResNet50V2 [62]	0.920	0.958	0.950	0.949
VGG16 [63]	0.960	1.000	1.000	1.000
Xception [64]	0.920	0.958	0.950	0.949
Custom CNN [54]	1.000	1.000	1.000	1.000

4.1. Classification Performance Metrics

Four critical performance metrics for multiclass classification—accuracy, precision, recall, and F1 score—were used to understand the effectiveness of the different DTL models along with a custom CNN model, accompanied by the models' training times. These metrics are reported in Table 3 for the 6-class dataset. They are pivotal in determining how well a model performs in classification tasks, where the balance among true positives, true negatives, false positives, and false negatives is crucial. Since the dataset is highly imbalanced (Section 3.1 Dataset Selection, mentioned above), it is appropriate to also present models' performance for the 5-class (minority/anomaly-only) dataset, as reported in Table 4.

The performance metrics demonstrate that among selected pre-trained DL models, the MobileNetV2 exhibits the highest F1 score (0.998) and accuracy (0.998), followed by InceptionV3 and VGG16, which both achieve an F1 score of 0.997 and accuracy of 0.998 in 6-class classification. Meanwhile, in 5-class classification, VGG16 excels in performance along with ConvNeXtTiny, DenseNet121, and NASNetMobile, attaining an F1 score of 1.000 and accuracy of 0.960 in performing the smart inspection of thermal anomalies, whereas the customized CNN ensembled model achieves a perfect F1 score (1.000) and accuracy (1.000). Furthermore, InceptionV3 exhibits the least training time (326 s) among selected pre-trained DL models, whereas the customized CNN ensembled model achieves an even lesser training time (204 s), which shows an efficient and fast model.

Moreover, the highly imbalanced dataset was made balanced by resampling the dataset (using Synthetic Minority Over-sampling Technique—SMOTE), having increased instances, i.e., Good: 2646, Junction box: 2647, Hotspot: 2647, Patchwork: 2647, Substring: 2647, and Multistring: 2647. The InceptionV3 model (training time: 1212 s) is trained with the dataset and achieved an accuracy, precision, recall, and F1 score of 1.000.

4.2. Explainable Predictions

The outcome of SmoothGrad with Guided Backpropagation visualizations is depicted in Figure 4. The pre-trained DL models correctly identified high-saliency regions over the areas having the highest temperature values in the patchwork and multistring cases.

The representations of predicted output features embedding are visually portrayed in Figure 5, with UMAP (Hellinger Metric) technique depicting definite clusters.

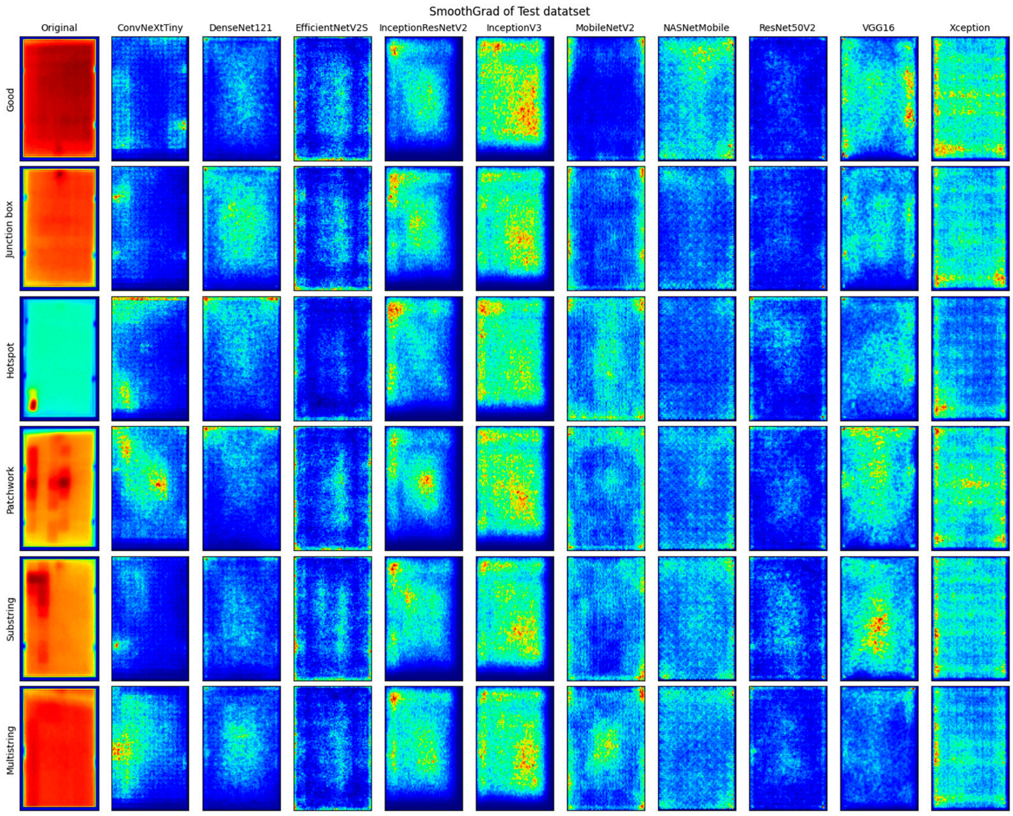

Figure 4. Explainable deep learning—SmoothGrad with Guided Backpropagation visualizations from the last convolutional layer for 6-class classification (jet colormap as pseudo-color applied for visual depiction). Red corresponds to higher activation values, blue to lower values.

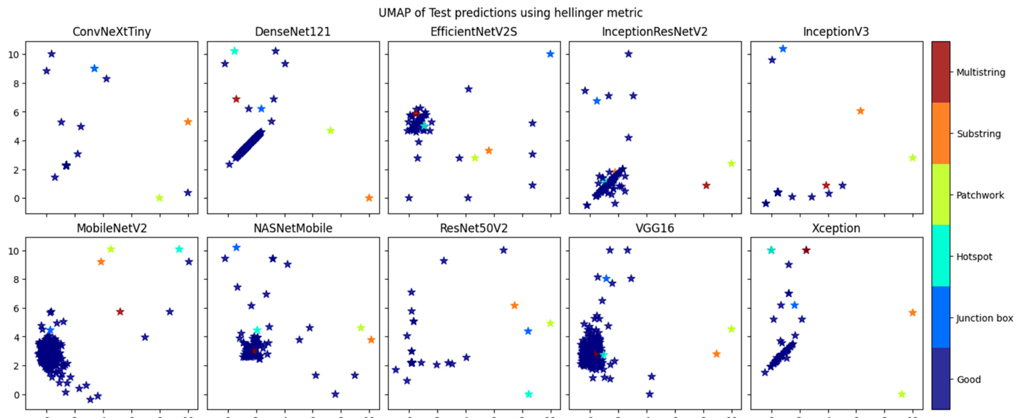

Figure 5. Embedding with UMAP (feature clustering) of test dataset predictions (Hellinger metric). Each data point is depicted as a star-shaped point. Kindly note that some points are overlapped.

4.3. Limitations

This case study has two main limitations. First, the number of available data instances belonging to each minority class is somehow insufficient to train and validate the hungry DTL models. This is because the targeted electric power output of SPV energy-generating assets is typically designed for healthy conditions, resulting in fewer occurrences of thermal anomalies. Thus, the DTL models struggle during the training process to achieve the correct diagnosis of thermal anomalies, resulting in lower multiclass classification accuracy compared to the customized CNN ensembled model.

Second, the resampling of the dataset, i.e., synthetic or generative oversampling, was employed only by the InceptionV3 model to test the model performance on a balanced dataset, resulting in a perfect F1 score (1.000) and accuracy (1.000). Although the objective was to assess the capability and strength of the pre-trained DL models on the adopted radiometric thermographic dataset comprising floating-point numerical values, resampling was avoided on other DTL models. Future studies could extend this work by utilizing a more diverse and larger dataset to investigate other pre-trained DL models with and without resampling, thereby achieving greater better generalizability and higher diagnostic accuracy outcomes.

5. Conclusions

Generally, the DTL models seem to be effective for multiclass classification when using standardized image datasets. Among the DTL models, MobileNetV2 exhibits the highest F1 score (0.998) and accuracy (0.998), followed by InceptionV3 and VGG16, with an F1 score of 0.997 and accuracy of 0.998 in 6-class classification. In 5-class (minority/anomaly-only) classification, VGG16 excels in performance, along with ConvNeXtTiny, DenseNet121, and NASNetMobile, attaining an F1 score of 1.000 and an accuracy of 0.960. Notably, the DTL model showing the fastest training time is InceptionV3 (326 s). However, the custom CNN ensembled model achieves a perfect F1 score (1.000) and accuracy (1.000) with the least training time (204 s). Furthermore, employing XAI techniques, i.e., SmoothGrad with Guided Backpropagation and UMAP, provided valuable insights into the operation of the pre-trained DL models on the adopted dataset (a floating-point temperature intensity matrix), visualized relevant high-temperature feature regions, and predicted features clustering, thereby enhancing cognitive understanding.

Overall, this work contributes to advancing the IRI system for thermographic vision inspection of SPV arrays under the PdM framework, which could further enhance SPV array performance by diagnosing potential thermal faults earlier. Indeed, early diagnosis is important for the economic life of large-scale (and utility-scale) SPV energy systems, helping assisting to protect their intensive capital investments in escalating global warming effects, particularly for effective humanitarian efforts.

Author Contributions: Conceptualization, U.R.Q., A.R. and N.A.; data curation, U.R.Q. and A.R.; formal analysis, U.R.Q., A.R. and N.A.; methodology, U.R.Q., A.R. and N.A.; resources, A.R., V.B. and M.L.S.; software, A.R.; supervision, N.A., V.B. and M.L.S.; validation, V.B. and M.L.S.; writing—original draft, U.R.Q., A.R. and N.A.; writing—review and editing, U.R.Q., A.R., N.A., V.B. and M.L.S. All authors have read and agreed to the published version of the manuscript.

Funding: The funding was sourced from the Italian Ministry of University and Research (CUP: D95F21002330006) for research doctorate programs (macro-areas of Sustainability and Innovation) under Ministerial Decree 1061 (10 August 2021) from the pool of resources dedicated to Research and Innovation, National Operational Program (NOP) 2014–2020 at Politecnico di Bari, Italy.

Data Availability Statement: The raw dataset used in this case study can be retrieved from [54].

Acknowledgments: U.R.Q. acknowledges the assistance of ChatGPT and Grammarly for light editing and grammar correction of this article.

Conflicts of Interest: The authors declare no conflicts of interest.

References

1. United Nations. *The Sustainable Development Goals Report 2024*; United Nations Statistics Division Development Data and Outreach Branch: New York, NY, USA, 2024. Available online: https://unstats.un.org/sdgs/report/2024 (accessed on 9 July 2024).
2. REN21. *Renewables 2024 Global Status Report Collection: Energy Supply*; EN21 Secretariat: Paris, France, 2024. Available online: https://www.ren21.net/gsr2024_SUPPLY_report/ (accessed on 9 July 2024).
3. United Nations. The Sustainable Development Goals Extended Report 2024 (Goal-7: Affordable and Clean Energy). 2024. Available online: https://unstats.un.org/sdgs/report/2024/extended-report/Extended-Report_Goal-7.pdf (accessed on 9 July 2024).

4. SolarPower Europe. Global Market Outlook for Solar Power 2024–2028. 2024. Available online: https://api.solarpowereurope.org/uploads/Global_Market_Outlook_for_Solar_Power_2024_a083b6dcd5.pdf (accessed on 10 July 2024).
5. Wiatros-Motyka, M.; Fulghum, N.; Jones, D. *Global Electricity Review 2024*; Ember: London, UK, 2024. Available online: https://ember-climate.org/insights/research/global-electricity-review-2024/ (accessed on 23 July 2024).
6. IRENA. Renewable Power Generation Costs in 2022. Abu Dhabi. 2023. Available online: https://www.irena.org/-/media/Files/IRENA/Agency/Publication/2023/Aug/IRENA_Renewable_power_generation_costs_in_2022.pdf (accessed on 11 July 2024).
7. EurObserv'ER Photovoltaic Barometer. 2024. Available online: https://www.eurobserv-er.org/photovoltaic-barometer-2024/ (accessed on 9 July 2024).
8. IRENA. *Renewable Capacity Statistics 2024*; International Renewable Energy Agency: Masdar City, Abu Dhabi, 2024. Available online: https://www.irena.org/-/media/Files/IRENA/Agency/Publication/2024/Mar/IRENA_RE_Capacity_Statistics_2024.pdf?rev=a587503ac9a2435c8d13e40081d2ec34 (accessed on 9 July 2024).
9. Brown, S.; Jones, D. *European Electricity Review 2024*; Ember: London, UK, 2024. Available online: https://ember-climate.org/insights/research/european-electricity-review-2024/ (accessed on 23 July 2024).
10. IEA. World Energy Investment 2024. 2024. Available online: https://www.iea.org/reports/world-energy-investment-2024/overview-and-key-findings (accessed on 17 July 2024).
11. Swiss Re. Changing Climates: The Heat Is (Still) On. Zurich. 2024. Available online: https://www.swissre.com/dam/jcr:cdbae8ed-24d0-4ec8-ad49-14f16846e556/2024-02-28-sri-expertise-publication-changing-climates-heat-still-on.pdf (accessed on 20 July 2024).
12. Copernicus Climate Change Service (C3S) Copernicus: 2023 Is the Hottest Year on Record. Available online: https://climate.copernicus.eu/copernicus-2023-hottest-year-record (accessed on 20 July 2024).
13. Copernicus Climate Change Service (C3S) Global Climate Highlights 2023. Available online: https://climate.copernicus.eu/global-climate-highlights-2023 (accessed on 20 July 2024).
14. Zachariah, M.; Clarke, B.; Vahlberg, M.; Pereira Marghidan, C.; Singh, R.; Sengupta, S.; Otto, F.; Pinto, I.; Mistry, M.; Arrighi, J.; et al. *Climate Change Made the Deadly Heatwaves That Hit Millions of Highly Vulnerable People across Large Parts of Asia More Frequent and Extreme*; World Weather Attribution (WWA), Imperial College London: London, UK, 2024. Available online: https://www.worldweatherattribution.org/climate-change-made-the-deadly-heatwaves-that-hit-millions-of-highly-vulnerable-people-across-asia-more-frequent-and-extreme/ (accessed on 20 July 2024).
15. Zachariah, M.; Philip, S.; Pinto, I.; Vahlberg, M.; Singh, R.; Otto, F.; Barnes, C.; Kimutai, J. *Extreme Heat in North America, Europe and China in July 2023 Made Much More Likely by Climate Change*; World Weather Attribution (WWA); Imperial College London: London, UK, 2023. Available online: https://www.worldweatherattribution.org/extreme-heat-in-north-america-europe-and-china-in-july-2023-made-much-more-likely-by-climate-change/ (accessed on 20 July 2024).
16. C3S. July 2023 Sees Multiple Global Temperature Records Broken. 2023. Available online: https://climate.copernicus.eu/july-2023-sees-multiple-global-temperature-records-broken (accessed on 21 July 2024).
17. C3S. The European Heatwave of July 2023 in a Longer-Term Context. 2023. Available online: https://climate.copernicus.eu/european-heatwave-july-2023-longer-term-context (accessed on 21 July 2024).
18. Van Oldenborgh, G.J.; Wehner, M.F.; Vautard, R.; Otto, F.E.L.; Seneviratne, S.I.; Stott, P.A.; Hegerl, G.C.; Philip, S.Y.; Kew, S.F. Attributing and Projecting Heatwaves Is Hard: We Can Do Better. *Earths Future* **2022**, *10*, e2021EF002271. [CrossRef]
19. WMO. Heatwave. Available online: https://wmo.int/topics/heatwave (accessed on 22 July 2024).
20. UNDRR. Heatwave. Available online: https://www.undrr.org/understanding-disaster-risk/terminology/hips/mh0047 (accessed on 22 July 2024).
21. UN OCHA. Global Humanitarian Overview 2024. 2023. Available online: https://www.unocha.org/publications/report/world/global-humanitarian-overview-2024-enarfres (accessed on 20 July 2024).
22. WMO. More Extreme Heat Demands Coordinated Action. 2024. Available online: https://reliefweb.int/report/world/more-extreme-heat-demands-coordinated-action (accessed on 15 July 2024).
23. IFRC; UN OCHA. Extreme Heat: Preparing for the Heatwaves of the Future. 2022. Available online: https://www.ifrc.org/document/extreme-heat-preparing-heat-waves-future (accessed on 16 July 2024).
24. WMO. State of the Global Climate 2023 (WMO-No. 1347). Available online: https://library.wmo.int/records/item/68835-state-of-the-global-climate-2023 (accessed on 15 July 2024).
25. UN OCHA. Asia and the Pacific: Heatwaves in South and South-East Asia (April 2024) as of 17 May 2024. 2024. Available online: https://www.unocha.org/publications/report/bangladesh/asia-and-pacific-heatwaves-south-and-south-east-asia-april-2024-17-may-2024 (accessed on 15 July 2024).
26. WWA. Climate Change Made Devastating Early Heat in India and Pakistan 30 Times More Likely. 2022. Available online: https://www.worldweatherattribution.org/climate-change-made-devastating-early-heat-in-india-and-pakistan-30-times-more-likely/ (accessed on 22 July 2024).

27. WWA. Extreme Humid Heat in South Asia in April 2023, Largely Driven by Climate Change, Detrimental to Vulnerable and Disadvantaged Communities. 2023. Available online: https://www.worldweatherattribution.org/extreme-humid-heat-in-south-asia-in-april-2023-largely-driven-by-climate-change-detrimental-to-vulnerable-and-disadvantaged-communities/ (accessed on 22 July 2024).
28. WWA. Climate Change and the Escalation of Global Extreme Heat: Assessing and Addressing the Risks. London, 2024. Available online: https://www.worldweatherattribution.org/heat-action-day-report-climate-change-and-the-escalation-of-global-extreme-heat/ (accessed on 16 July 2024).
29. WWA. Extreme Heat Killing More than 100 People in Mexico Hotter and Much More Likely Due to Climate Change. 2024. Available online: https://www.worldweatherattribution.org/extreme-heat-killing-more-than-100-people-in-mexico-hotter-and-much-more-likely-due-to-climate-change/ (accessed on 21 July 2024).
30. Boyle, C.; Mudd, G.; Mihelcic, J.R.; Anastas, P.; Collins, T.; Culligan, P.; Edwards, M.; Gabe, J.; Gallagher, P.; Handy, S.; et al. Delivering Sustainable Infrastructure That Supports the Urban Built Environment. *Environ. Sci. Technol.* **2010**, *44*, 4836–4840. [CrossRef] [PubMed]
31. IEA. *Unlocking Smart Grid Opportunities in Emerging Markets and Developing Economies*; IEA: Paris, France, 2023. Available online: https://www.iea.org/reports/unlocking-smart-grid-opportunities-in-emerging-markets-and-developing-economies (accessed on 23 July 2024).
32. IEA. *Electricity 2024: Analysis and Forecast to 2026*; IEA: Paris, France, 2024. Available online: https://managenergy.ec.europa.eu/publications/electricity-2024-analysis-and-forecast-2026_en (accessed on 23 July 2024).
33. Brás, T.A.; Simoes, S.G.; Amorim, F.; Fortes, P. How Much Extreme Weather Events Have Affected European Power Generation in the Past Three Decades? *Renew. Sustain. Energy Rev.* **2023**, *183*, 113494. [CrossRef]
34. Poddar, S.; Rougieux, F.; Evans, J.P.; Kay, M.; Prasad, A.A.; Bremner, S.P. Accelerated Degradation of Photovoltaic Modules under a Future Warmer Climate. *Prog. Photovolt. Res. Appl.* **2024**, *32*, 456–467. [CrossRef]
35. *BS EN 13306:2017*; Maintenance—Maintenance Terminology. BSI Standards Limited: London, UK, 2018. Available online: https://knowledge.bsigroup.com/products/maintenance-maintenance-terminology?version=standard (accessed on 24 April 2023).
36. Ahmed, W.; Ali, M.U.; Mahmud, M.A.P.; Niazi, K.A.K.; Zafar, A.; Kerekes, T. A Comparison and Introduction of Novel Solar Panel's Fault Diagnosis Technique Using Deep-Features Shallow-Classifier through Infrared Thermography. *Energies* **2023**, *16*, 1043. [CrossRef]
37. *IEC TS 62446-3:2017*; Photovoltaic (PV) Systems—Requirements for Testing, Documentation and Maintenance—Part 3: Photovoltaic Modules and Plants—Outdoor Infrared Thermography. 1.0. IEC: Geneva, Switzerland, 2017. Available online: https://webstore.iec.ch/en/publication/28628 (accessed on 3 February 2024).
38. Deng, J.; Dong, W.; Socher, R.; Li, L.-J.; Li, K.; Li, F.-F. ImageNet: A Large-Scale Hierarchical Image Database. In Proceedings of the 2009 IEEE Conference on Computer Vision and Pattern Recognition (CVPR 2009), Miami, FL, USA, 20–25 June 2009; pp. 248–255.
39. Sepúlveda-Oviedo, E.H.; Travé-Massuyès, L.; Subias, A.; Pavlov, M.; Alonso, C. Fault Diagnosis of Photovoltaic Systems Using Artificial Intelligence: A Bibliometric Approach. *Heliyon* **2023**, *9*, e21491. [CrossRef]
40. Liu, H.; Perera, A.; Al-Naji, A.; Boubaker, S.; Kamel, S.; Ghazouani, N.; Mellit, A. Assessment of Machine and Deep Learning Approaches for Fault Diagnosis in Photovoltaic Systems Using Infrared Thermography. *Remote Sens.* **2023**, *15*, 1686. [CrossRef]
41. Haidari, P.; Hajiahmad, A.; Jafari, A.; Nasiri, A. Deep Learning-Based Model for Fault Classification in Solar Modules Using Infrared Images. *Sustain. Energy Technol. Assess.* **2022**, *52*, 102110. [CrossRef]
42. Ahmed, W.; Hanif, A.; Kallu, K.D.; Kouzani, A.Z.; Ali, M.U.; Zafar, A. Photovoltaic Panels Classification Using Isolated and Transfer Learned Deep Neural Models Using Infrared Thermographic Images. *Sensors* **2021**, *21*, 5668. [CrossRef]
43. Azari, M.S.; Flammini, F.; Santini, S.; Caporuscio, M. A Systematic Literature Review on Transfer Learning for Predictive Maintenance in Industry 4.0. *IEEE Access* **2023**, *11*, 12887–12910. [CrossRef]
44. Russakovsky, O.; Deng, J.; Su, H.; Krause, J.; Satheesh, S.; Ma, S.; Huang, Z.; Karpathy, A.; Khosla, A.; Bernstein, M.; et al. ImageNet Large Scale Visual Recognition Challenge. *Int. J. Comput. Vis.* **2015**, *115*, 211–252. [CrossRef]
45. Le, M.; Van Su, L.; Dang Khoa, N.; Dao, V.D.; Ngoc Hung, V.; Hong Ha Thi, V. Remote Anomaly Detection and Classification of Solar Photovoltaic Modules Based on Deep Neural Network. *Sustain. Energy Technol. Assess.* **2021**, *48*, 101545. [CrossRef]
46. Korkmaz, D.; Acikgoz, H. An Efficient Fault Classification Method in Solar Photovoltaic Modules Using Transfer Learning and Multi-Scale Convolutional Neural Network. *Eng. Appl. Artif. Intell.* **2022**, *113*, 104959. [CrossRef]
47. Duranay, Z.B. Fault Detection in Solar Energy Systems: A Deep Learning Approach. *Electronics* **2023**, *12*, 4397. [CrossRef]
48. Pamungkas, R.F.; Utama, I.B.K.Y.; Jang, Y.M. A Novel Approach for Efficient Solar Panel Fault Classification Using Coupled UDenseNet. *Sensors* **2023**, *23*, 4918. [CrossRef]
49. Ahmed, W. Enhancing Solar PV Reliability with Hybrid Local Features and Infrared Thermography. *Energy Rep.* **2025**, *13*, 345–352. [CrossRef]
50. Ramadan, E.A.; Moawad, N.M.; Abouzalm, B.A.; Sakr, A.A.; Abouzaid, W.F.; El-Banby, G.M. An Innovative Transformer Neural Network for Fault Detection and Classification for Photovoltaic Modules. *Energy Convers. Manag.* **2024**, *314*, 118718. [CrossRef]

51. Mellit, A.; Moussaoui, C.; Pastore, S.; Pavan, A.M. Fault Diagnosis of Photovoltaic Modules Using Infrared Images and Hybrid DCNNs: A Comparative Study. In Proceedings of the 2024 IEEE International Conference on Environment and Electrical Engineering and 2024 IEEE Industrial and Commercial Power Systems Europe (EEEIC/I&CPS Europe 2024), Rome, Italy, 17–20 June 2024.
52. Ksira, Z.; Mellit, A.; Blasuttigh, N.; Massi Pavan, A. A Novel Embedded System for Real-Time Fault Diagnosis of Photovoltaic Modules. *IEEE J. Photovolt.* **2024**, *14*, 354–362. [CrossRef]
53. Wang, B.; Chen, Q.; Wang, M.; Chen, Y.; Zhang, Z.; Liu, X.; Gao, W.; Zhang, Y.; Zhang, H. PVF-10: A High-Resolution Unmanned Aerial Vehicle Thermal Infrared Image Dataset for Fine-Grained Photovoltaic Fault Classification. *Appl. Energy* **2024**, *376*, 124187. [CrossRef]
54. Qureshi, U.R.; Rashid, A.; Altini, N.; Bevilacqua, V.; La Scala, M. Radiometric Infrared Thermography of Solar Photovoltaic Systems: An Explainable Predictive Maintenance Approach for Remote Aerial Diagnostic Monitoring. *Smart Cities* **2024**, *7*, 1261–1288. [CrossRef]
55. Liu, Z.; Mao, H.; Wu, C.-Y.; Feichtenhofer, C.; Darrell, T.; Xie, S. A ConvNet for the 2020s. In Proceedings of the 2022 IEEE/CVF Conference on Computer Vision and Pattern Recognition (CVPR), New Orleans, LA, USA, 18–24 June 2022; IEEE: New York, NY, USA, 2022; pp. 11966–11976.
56. Huang, G.; Liu, Z.; Van Der Maaten, L.; Weinberger, K.Q. Densely Connected Convolutional Networks. In Proceedings of the 30th IEEE Conference on Computer Vision and Pattern Recognition, CVPR 2017, Honolulu, HI, USA, 21–26 July 2017; pp. 2261–2269.
57. Tan, M.; Le, Q.V. EfficientNetV2: Smaller Models and Faster Training. *Proc. Mach. Learn. Res.* **2021**, *139*, 10096–10106.
58. Szegedy, C.; Vanhoucke, V.; Ioffe, S.; Shlens, J.; Wojna, Z. Rethinking the Inception Architecture for Computer Vision. In Proceedings of the 2016 IEEE Conference on Computer Vision and Pattern Recognition (CVPR), Las Vegas, NV, USA, 27–30 June 2016; pp. 2818–2826.
59. Szegedy, C.; Ioffe, S.; Vanhoucke, V.; Alemi, A. Inception-v4, Inception-ResNet and the Impact of Residual Connections on Learning. In Proceedings of the 31st AAAI Conference on Artificial Intelligence (AAAI 2017), San Francisco, CA, USA, 4–9 February 2017; pp. 4278–4284.
60. Sandler, M.; Howard, A.; Zhu, M.; Zhmoginov, A.; Chen, L.-C. MobileNetV2: Inverted Residuals and Linear Bottlenecks. In Proceedings of the 2018 IEEE/CVF Conference on Computer Vision and Pattern Recognition, Salt Lake City, UT, USA, 18–22 June 2018; pp. 4510–4520.
61. Zoph, B.; Vasudevan, V.; Shlens, J.; Le, Q.V. Learning Transferable Architectures for Scalable Image Recognition. In Proceedings of the 2018 IEEE/CVF Conference on Computer Vision and Pattern Recognition, Salt Lake City, UT, USA, 21–26 July 2018; pp. 8697–8710.
62. He, K.; Zhang, X.; Ren, S.; Sun, J. Identity Mappings in Deep Residual Networks. In Proceedings of the 14th European Conference on Computer Vision (ECCV 2016—Part IV), Amsterdam, The Netherlands, 11–14 October 2016; Volume 9908, pp. 630–645.
63. Simonyan, K.; Zisserman, A. Very Deep Convolutional Networks for Large-Scale Image Recognition. In Proceedings of the 3rd International Conference on Learning Representations (ICLR 2015), San Diego, CA, USA, 7–9 May 2015.
64. Chollet, F. Xception: Deep Learning with Depthwise Separable Convolutions. In Proceedings of the 30th IEEE Conference on Computer Vision and Pattern Recognition (CVPR 2017), Honolulu, HI, USA, 21–26 July 2017; pp. 1800–1807.
65. Bhuiyan, M.R.; Uddin, J. Deep Transfer Learning Models for Industrial Fault Diagnosis Using Vibration and Acoustic Sensors Data: A Review. *Vibration* **2023**, *6*, 218–238. [CrossRef]
66. Asif, S.; Zhao, M.; Tang, F.; Zhu, Y. A Deep Learning-Based Framework for Detecting COVID-19 Patients Using Chest X-rays. *Multimed. Syst.* **2022**, *28*, 1495–1513. [CrossRef] [PubMed]
67. Chen, X.; Liang, C.; Huang, D.; Real, E.; Wang, K.; Liu, Y.; Pham, H.; Dong, X.; Luong, T.; Hsieh, C.-J.; et al. Symbolic Discovery of Optimization Algorithms. In Proceedings of the 37th Conference on Neural Information Processing Systems (NeurIPS 2023), New Orleans, LA, USA, 10–16 December 2023; pp. 49205–49233.
68. Keras. Lion Optimizer. Available online: https://keras.io/api/optimizers/lion/ (accessed on 3 February 2025).
69. Minh, D.; Wang, H.X.; Li, Y.F.; Nguyen, T.N. Explainable Artificial Intelligence: A Comprehensive Review. *Artif. Intell. Rev.* **2021**, *55*, 3503–3568. [CrossRef]
70. Mohamed, E.; Sirlantzis, K.; Howells, G. A Review of Visualisation-as-Explanation Techniques for Convolutional Neural Networks and Their Evaluation. *Displays* **2022**, *73*, 102239. [CrossRef]
71. Linardatos, P.; Papastefanopoulos, V.; Kotsiantis, S. Explainable AI: A Review of Machine Learning Interpretability Methods. *Entropy* **2021**, *23*, 18. [CrossRef]
72. Tjoa, E.; Guan, C. A Survey on Explainable Artificial Intelligence (XAI): Toward Medical XAI. *IEEE Trans. Neural Netw. Learn. Syst.* **2021**, *32*, 4793–4813. [CrossRef]
73. Hussain, S.M.; Buongiorno, D.; Altini, N.; Berloco, F.; Prencipe, B.; Moschetta, M.; Bevilacqua, V.; Brunetti, A. Shape-Based Breast Lesion Classification Using Digital Tomosynthesis Images: The Role of Explainable Artificial Intelligence. *Appl. Sci.* **2022**, *12*, 6230. [CrossRef]

74. Simonyan, K.; Vedaldi, A.; Zisserman, A. Deep Inside Convolutional Networks: Visualising Image Classification Models and Saliency Maps. In Proceedings of the 2nd International Conference on Learning Representations (ICLR 2014)—Workshop Track, Banff, AB, Canada, 14–16 April 2014.
75. Smilkov, D.; Thorat, N.; Kim, B.; Viégas, F.; Wattenberg, M. SmoothGrad: Removing Noise by Adding Noise. Available online: https://arxiv.org/pdf/1706.03825 (accessed on 3 February 2025).
76. Springenberg, J.T.; Dosovitskiy, A.; Brox, T.; Riedmiller, M. Striving for Simplicity: The All Convolutional Net. In Proceedings of the 3rd International Conference on Learning Representations (ICLR 2015)—Workshop Track, San Diego, CA, USA, 7–9 May 2014.
77. McInnes, L.; Healy, J.; Melville, J. UMAP: Uniform Manifold Approximation and Projection for Dimension Reduction. *arXiv* **2018**, arXiv:1802.03426.